Superconducting Qubits above 20 GHz Operating over 200 mK

Alexander Anferov[1,2,*] Shannon P. Harvey[3,4] Fanghui Wan[3,4] Jonathan Simon,[3,5] and David I. Schuster[3,4,†]

[1]*James Franck Institute, University of Chicago, Chicago, Illinois 60637, USA*
[2]*Department of Physics, University of Chicago, Chicago, Illinois 60637, USA*
[3]*Department of Applied Physics, Stanford University, Stanford, California 94305, USA*
[4]*SLAC National Accelerator Laboratory, Menlo Park, California 94025, USA*
[5]*Department of Physics, Stanford University, Stanford, California 94305, USA*

Current state-of-the-art superconducting microwave qubits are cooled to extremely low temperatures to avoid sources of decoherence. Higher qubit operating temperatures would significantly increase the cooling power available, which is desirable for scaling up the number of qubits in quantum computing architectures and integrating qubits in experiments requiring increased heat dissipation. To operate superconducting qubits at higher temperatures, it is necessary to address both quasiparticle decoherence (which becomes significant for aluminum junctions above 160 mK) and dephasing from thermal microwave photons (which are problematic above 50 mK). Using low-loss niobium-trilayer junctions, which have reduced sensitivity to quasiparticles due to the higher superconducting transition temperature of niobium, we fabricate transmons with higher frequencies than previously studied, up to 24 GHz. We measure decoherence and dephasing times of about 1 μs, corresponding to average qubit quality factors of approximately 10^5, and find that decoherence is unaffected by quasiparticles up to 1 K. Without relaxation from quasiparticles, we are able to explore dephasing from purely thermal sources, finding that our qubits can operate up to approximately 250 mK while maintaining similar performance. The thermal resilience of these qubits creates new options for scaling up quantum processors, enables hybrid quantum experiments with high heat-dissipation budgets, and introduces a material platform for even-higher-frequency qubits.

I. INTRODUCTION

Superconducting qubits built from Josephson junctions are a promising technology for quantum sensing, hybrid systems coupling different types of quantum emitters [1,2], and realizing large-scale quantum computing architectures [3]. While current qubits typically operate below 10 GHz due to widely available cryogenic microwave equipment, increased frequencies expand the range of accessible energies in quantum experiments, can couple to a new range of signals and quantum emitters, and, importantly, enable higher operating temperatures. This offers a straightforward approach for scalability by making use of the significantly higher cooling power available with even a moderate increase in temperature [4]. Thermally resilient qubits could reduce hardware overheads for microwave quantum interconnects [5,6], provide new opportunities for direct integration with superconducting digital logic [7–9], and help manage the heat load from expanding numbers of qubit control lines [10], as superconducting quantum processors [11–13] expand beyond hundreds of qubits. For hybrid quantum systems [1,2], many of which introduce additional challenges by exposing qubits to magnetic fields or direct optical illumination [14–17], more resilient qubits could also help reduce experiment complexity and improve performance.

Increasing the qubit operating temperature requires a two-pronged approach addressing both increased environmental radiation as well as quasiparticle loss. Specifically, thermal photons at the qubit frequency result in heating, requiring active reset [18,19] or extensive dissipation engineering [20,21] to artificially cool the qubit to its ground state before experiments begin. Furthermore, the thermal population in the readout resonator (less easily cooled [22]) induces qubit dephasing [23]. Increasing system frequencies mitigate these effects due to the reduced thermal

*Contact author: aanferov@uchicago.edu
†Contact author: dschus@stanford.edu

sensitivity of higher-energy photons and expands accessible operating temperatures and cooling powers even for conventional aluminum Josephson-junction qubits [3,24].

Ultimately, the operating temperatures are limited by decoherence from quasiparticles [25–30] in the super-conductor. The higher energy gap of niobium relative to that of aluminum results in a significantly lower quasiparticle density at elevated temperatures as well as increased nonequilibrium quasiparticle recombination rates [31], making it a promising material for realizing higher-temperature qubits and increasing repetition rates for optical-transduction experiments [14–17]. Full temperature resilience requires replacing aluminum junctions with a high-temperature nonlinear element, which can be realized with newly optimized niobium nitride [32] or niobium-based [33] junctions: along with increased plasma frequencies [34] that simplify the high-frequency qubit design, these junctions have shown rapidly improving coherence properties in microwave qubits and reduced quasiparticle sensitivity [33].

In this work, we scale up transmon qubits to 11–24 GHz, expanding the frequency range studied with superconducting devices. Using micron-scale optically defined niobium-trilayer Josephson junctions, we achieve qubit dephasing times above 1 μs through material improvements and residue-removal techniques. With higher frequencies and the quasiparticle insensitivity of niobium, we improve the qubit thermal resilience, demonstrating coherent behavior above 200 mK, and investigate their coherence properties up to 1 K in a previously unexplored regime.

II. HIGH-FREQUENCY QUBIT DESIGN

The key element at the heart of our transmon qubit is a niobium-trilayer Josephson junction with a high critical-current density (J_c), shown in Fig. 1(a). We use a self-aligned fabrication process (see Appendix A) to form a Nb/Al,AlO$_x$/Al/Nb Josephson junction on a C-plane sapphire substrate, with two main changes from Ref. [33]. First, we use low-temperature plasma-enhanced chemical vapor deposition (PECVD) for growing the SiO$_2$ spacer [35]: keeping the wafer below 230 °C during the growth process creates a spacer oxide with lower loss than other methods such as high-density PECVD [33] (for more details, see Appendix B) and preserves a high J_c density needed for higher-frequency junctions. Second, immediately prior to measurement, we use a 72 ± 1 °C solution of catechol, hydroxylamine, and 2-(2-aminoethylamine)-ethanol (Dupont EKC 265) to remove lossy plasma-etch residues along with a thin layer of the oxidized niobium surface, known to contain lossy oxides [36,37]. This treatment (see Appendix B) leaves a smooth metal surface with minimal defects and residues. For these PECVD junctions, the J_c density can be adjusted between 0.1 and 2.6 kA/cm^2

(see Appendix C). Although higher densities are possible, we select a J_c between 0.19 and 0.36 kA/cm^2, which is closer to that of typical aluminum junctions (typically 0.05 kA/cm^2 [38]), allowing us to design qubits between 11 and 24 GHz using junction-finger dimensions between 0.4 and 0.8 μm, achieved entirely with optical lithography. We note that the junction reproducibility and minimum feature size could also be improved with electron-beam lithography.

Our qubit geometry, shown in Fig. 1(b), is qualitatively similar to that for conventional microwave transmon qubits [39,40], with the primary difference that every major feature is slightly smaller. The rounded cross-shaped qubit capacitor C_Q is capacitively coupled to a (20–22)-GHz quarter-wave coplanar waveguide resonator used for dispersive measurements. The other end of the resonator is inductively coupled ($\kappa/2\pi = 2$–9 MHz) to a common feed line. The system can be modeled by the circuit in Fig. 1(c), where the qubit frequency is determined by the Josephson inductance L_J and total shunt capacitance C_Σ. As with linear circuits, reducing the capacitance and inductance increases the qubit frequency. A smaller capacitance has the benefit of increased anharmonicity and thus faster possible qubit control operations, which can help improve single-qubit gate fidelities. While this speed-up could be exploited until the device begins to approach the
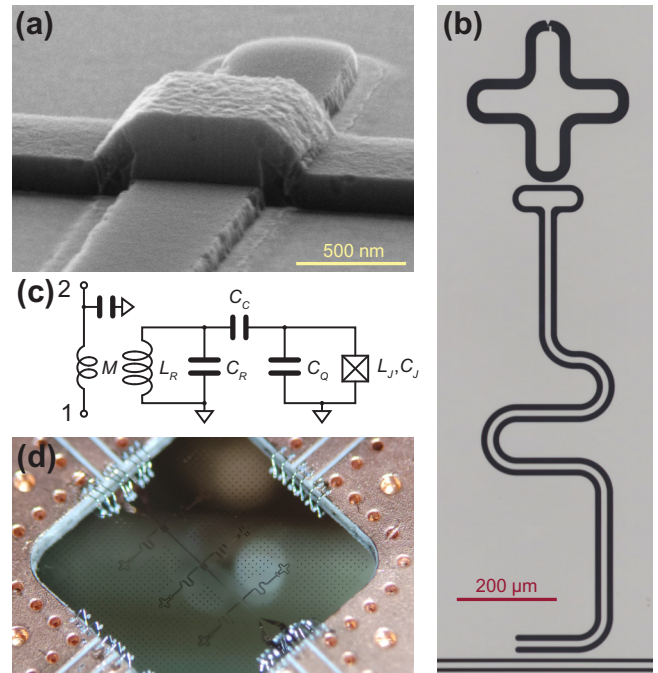
FIG. 1. The qubit geometry. (a) A scanning electron micrograph of a low-loss niobium-trilayer junction at the core of the qubit. (b) A micrograph of the qubit and readout-resonator geometry, with the junction location marked at the top. (c) The equivalent circuit of the qubit and readout resonator coupled inductively to a transmission line. (d) A photograph of a chip containing six qubits mounted in a low-loss K-band circuit board.

charge-sensitive regime [27], because the qubits reported in this paper use optical lithography, they have a large capacitance that limits the anharmonicity and therefore the gate speeds. However, designing 20-GHz qubits with lower capacitance will enable substantially faster gate times than achievable with microwave qubits.

The qubit capacitor, ground plane, and readout resonator are defined along with the junction, so no additional fabrication steps are needed. Chips with several qubits and their readout resonators sharing a common microwave feed line are patterned on 5-mm-square chips, and mounted in a K-band [(18–27)-GHz] package shown in Fig. 1(d), which is carefully engineered for low-loss and mode-free operation up to 30 GHz (see Appendix D). The assembly is thermalized to the base stage of a dilution refrigerator (65–95 mK), where transmission measurements through the central feed line can be used to control and measure the qubits [39,41].

III. QUBIT CHARACTERIZATION

The qubit properties are experimentally determined with microwave spectroscopy [39,42]. While monitoring low-power transmission through the system at the readout-resonator frequency, simultaneously applying a second probe pulse reveals the energy spectrum of the qubit, as shown in Fig. 2(a). At low powers, we observe a deflection in transmission at the bare qubit frequency f_{ge} as the qubit is excited, resulting in a dispersive shift of the resonator frequency. Increasing the power of the probe

pulse reveals the higher-energy states of the qubit through two-photon processes $f_{gf} = (f_{ge} + f_{ef})/2$ and excited-state transitions f_{ef}. This allows us to measure the anharmonicity $\alpha \equiv f_{ef} - f_{ge}$, which for our qubits is typically near 200 MHz. Notably, this level spacing (which sets an upper bound on qubit gate speed) is similar to that for many conventional microwave qubits [39,40,42] but could easily be adjusted in our design by picking a different junction J_c density or capacitor size.

A. Time-domain measurements

Next, we control the qubit. We apply fixed-length ($\sigma = 25$ ns) Gaussian pulses at the qubit frequency f_{ge} with varying amplitude (over which we have much finer control than for time), which results in sinusoidal behavior as shown in Fig. 2(b). We repeat this measurement with $\sigma = 60$ ns while varying pulse detuning from the transition $\Delta = f - f_{ge}$ and summarize the results in Fig. 2(c), where the brighter colors indicate the system in the excited state. At the qubit frequency, we observe a series of bright fringes; however, as the detuning from the transition increases, the oscillation rate increases, while the oscillation amplitude is quickly suppressed. The bandwidth of the fringes is further reduced by the finite nature of the pulse envelope [43–45].

To verify the time dependence of the Rabi oscillations, we also repeat this measurement at $\Delta = 0$ while varying σ and plot the results in Fig. 2(d). The observed fringes are evenly spaced for fixed amplitude (vertical slice) or
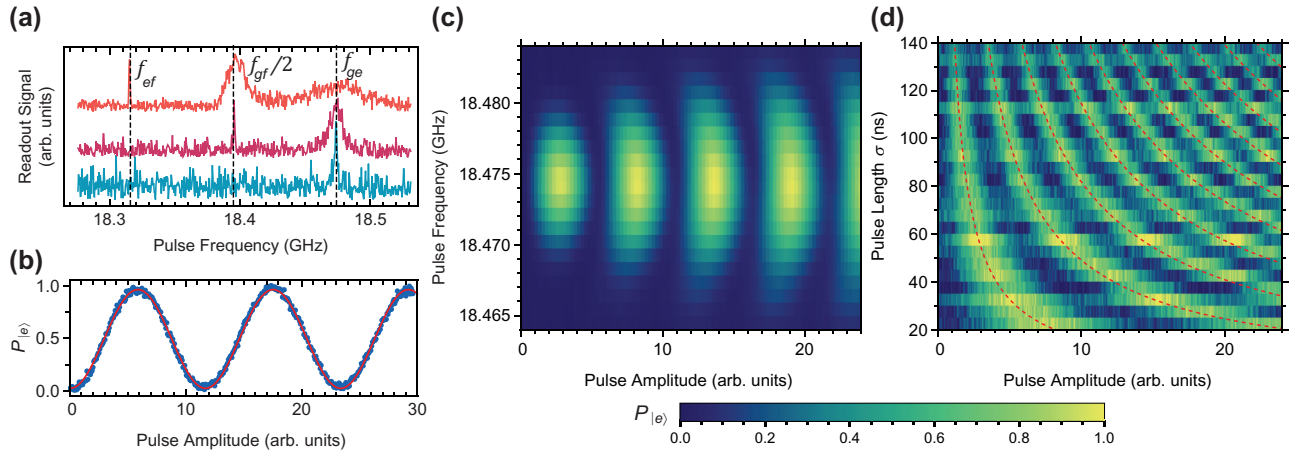

FIG. 2. The qubit dynamics. (a) Deflection of the readout-resonator transmission signal as a function of the applied qubit pulse frequency, shown for increasing qubit pulse power. At low powers (blue), a single peak is observed when the pulse is resonant with the qubit frequency ($f_{ge} = 18.474$ GHz). As the power increases, the line width of this transition increases and additional peaks appear due to excitations into higher qubit levels through many-photon excitations ($f_{gf}/2$ etc.). These features have a spacing of $\alpha/2 = (f_{ge} - f_{ef})/2$. (b) The measured excited-state probability shows Rabi oscillations when a fixed-length pulse with varying amplitude is applied at the qubit frequency. The red line is a fit to the expected sinusoidal behavior. (c) Rabi oscillations measured for frequencies near f_{ge}, with brighter colors corresponding to higher excited-state probabilities. Away from the transition frequency, the Rabi frequency increases while the oscillation amplitude decreases and becomes power dependent. (d) Rabi oscillations as a function of the pulse amplitude and length σ, with brighter colors corresponding to higher excited-state probabilities. The dashed red lines mark contours of integer π pulses, where $\sigma\Omega = m\pi$.

fixed length (horizontal): by fitting the fringe contours, we find Rabi rates as high as 100 MHz and calibrate a qubit π control pulse with σ between 20 and 40 ns. Since the bandwidth of these pulses is still much smaller than the level spacing, our single-qubit gate speeds could be optimized to be significantly shorter [46]. Further reducing our junction area and qubit capacitance to increase qubit anharmonicity could allow for even faster gate operation.

B. Coherence properties

We can now study the qubit relaxation time and the dephasing time, which dictate the qubit limitations and act as sensitive probes of loss channels. Fitting the characteristic population relaxation time T_1 [as shown in Fig. 3(a)] for each qubit, we find that T_1 roughly scales inversely with frequency as shown in Fig. 3(c), with $T_1 = 1.6\,\mu s$ for our best device. We find that T_1 typically fluctuates with a relative deviation of about 6% from the average value (see Appendix G), likely due to coupled two-level systems [47–49]. We note that hardware limitations prevent time-domain measurements of some of the qubits with frequencies outside the mixer bands (wafers A and C) or those overlapping with the readout resonators at approximately 21 GHz (wafer B). The highest-frequency qubits (e.g., wafer C) are above their readout-resonator frequencies (approximately 22 GHz), so are likely further affected by Purcell loss.

To probe the loss channels in detail, we use the frequency-independent qubit quality factor $Q_1 = 2\pi f_q T_1$, which we find for our devices is just below 10^5. Our K-band qubit quality factors are comparable to those for transmons made with a similar junction process,

which measure an average $Q_1 = 2.5 \times 10^5$ [33]. The slight decrease in our average Q_1 could be attributed to slightly higher junction [33] and surface participation [50] arising from our smaller qubit-capacitor size relative to the junction area. By comparison, state-of-the-art aluminum-junction microwave qubits now achieve quality factors of several million [24]. Having addressed potential loss from fluorocarbon residues, we expect that our qubit coherence is now likely primarily limited by loss in residual spacer material [see Fig. 1(a)] and potentially two-level systems in the relatively large junction-barrier region [51,52]. This suggests that future devices could be directly improved with smaller junctions and larger capacitor geometry, or with improved junction-fabrication techniques [32] and spacer-removal methods [53]. The quantum decoherence and material properties in this frequency range are still relatively unexplored, warranting further investigation [54] into the nature and sources of loss.

We also perform a Ramsey experiment to measure the dephasing time T_2^* and a Hahn-echo experiment to characterize the spin-echo dephasing time T_2 [Fig. 3(b)]. We find that T_2^* is consistently higher than T_1, nearing the dissipation limit $2T_1$. This suggests that the pure-dephasing rates are relatively low, which is expected from the low photon occupation of the higher-frequency readout resonators. The T_2 values, which add an additional π pulse to decouple the qubit from low-frequency noise, are not significantly different from T_2^*. For qubits with lower T_1 values (such as qubit B4), the Hahn echo reduces the visibility of qubit oscillations to the extent that it is no longer possible to reliably measure T_2. This implies that our qubit performance is primarily limited by dissipation (T_1) in the qubit and junction materials.
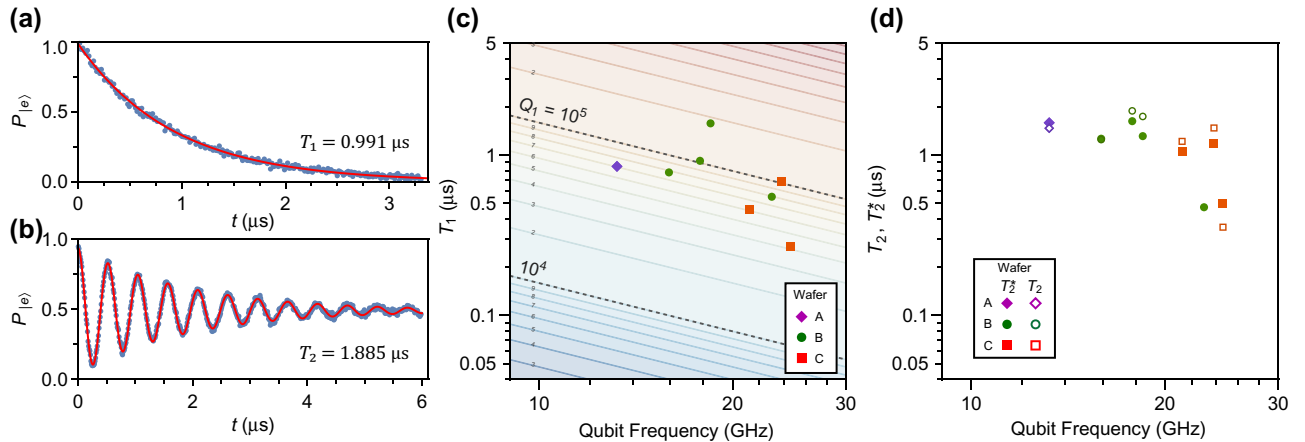

FIG. 3. The qubit coherence at 60 mK. (a) The average qubit decay time T_1 extracted by fitting the decay of excited-state population. (b) A Ramsey-dephasing experiment, from which the dephasing time T_2^* is extracted by fitting the exponential decay of the oscillations. (c) T_1 plotted as a function of the qubit frequency, grouped by wafer. The background color and numbered lines indicate the qubit quality factor $Q_1 = \omega_q T_1$. We find an overall mean Q_1 of 0.792×10^5, with some wafer-to-wafer variation. (d) T_2^* (filled points) and the Hahn-echo dephasing time T_2 (hollow points) for the qubits studied. We find an average T_2^* and T_2 of 1.124 μs and 1.357 μs, respectively.

IV. QUBIT SENSITIVITY TO ITS ENVIRONMENT

A key benefit of higher-frequency qubits is a reduced thermal occupation of higher energy levels, reducing initialization errors and minimizing the need for active reset [18,19]. We measure the residual excited-state population following the method in Ref. [55], as shown in Fig. 4. We perform Rabi oscillations between the e and f states by applying a Gaussian pulse of varying amplitude at the transition frequency f_{ef} [see Fig. 2(a)]. This measurement is also repeated with the g and e populations swapped with a ge π pulse immediately prior, resulting in a significantly stronger signal. For maximum contrast, the readout signal is projected to resolve the e and f states (rather than ge) for both measurements. By comparing the relative oscillation amplitudes, we obtain a thermal excited-state population of $0.017 \pm 0.004\%$, which is nearly an order of magnitude lower than values measured for microwave devices [55]. We note that the precision of this measurement is limited by our readout fidelity, which could be greatly improved by a K-band quantum limited amplifier [56,57]. This population corresponds to an effective qubit temperature [55] of 116 mK, which is significantly higher than the physical fridge temperature, suggesting that improved filtering [22,58] could help reduce these qubit initialization error rates even further.

A. Thermal dependence of coherence

To probe the thermal resilience of our qubits, we investigate our qubits at increased operating temperatures, shown in Fig. 5(a). We observe a small decrease in T_1 with temperature above 300 mK, consistent with qubit heating from its environment [59], but, importantly, we do not see the drastic temperature dependence seen in qubits with aluminum junctions due to quasiparticle-induced loss
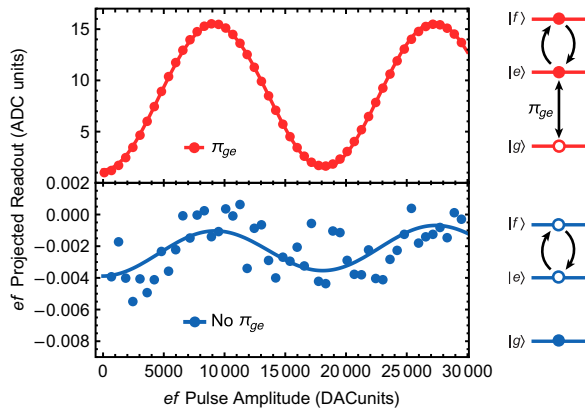

FIG. 4. The qubit thermal population. The residual e-state population of qubit C1, measured by comparing the ef Rabi-oscillation amplitude with g and e swapped (pink) and idle populations (blue). From this measurement, we find a probability of $0.017 \pm 0.004\%$ of finding the qubit in its excited state.
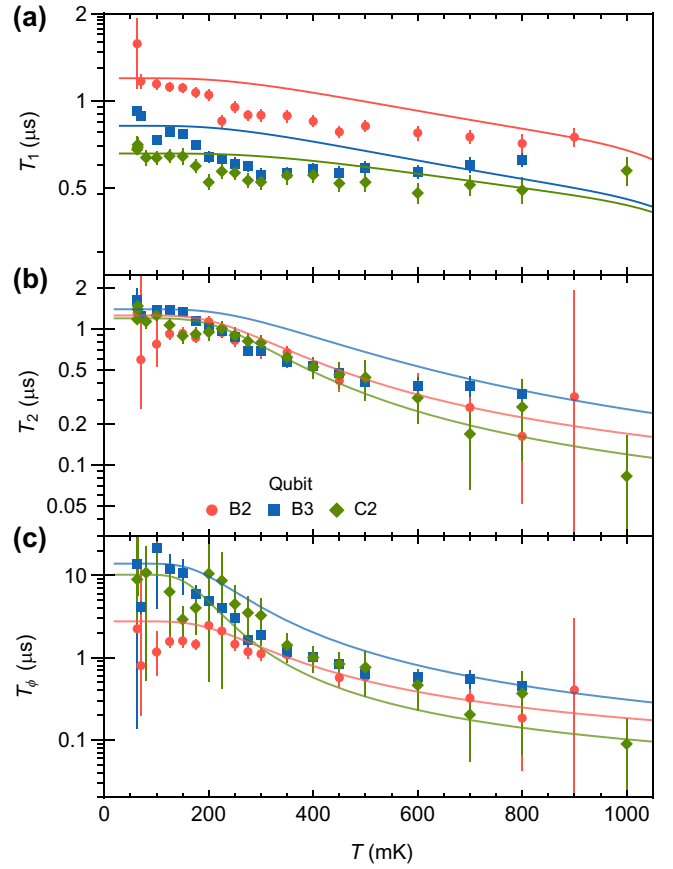

FIG. 5. Thermal decoherence and dephasing. (a) The decoherence time T_1 of three representative qubits measured as a function of the temperature. A mild decrease is observed at higher temperature, consistent with a model including loss from an increased system bath temperature (solid lines). (b) The Ramsey-dephasing time T_2^* as a function of the temperature. The behavior is largely captured by a parameter-free thermal dephasing model assuming a fixed T_1 (solid lines). (c) The pure-dephasing rate Γ_ϕ, which has dephasing from relaxation subtracted, resulting in better agreement with the model.

[27–29], in line with expectations for niobium. The measured dephasing time shown in Fig. 5(b) does not significantly decrease until above 200 mK and is captured with the following parameter-free model for dephasing from thermal photons in the readout resonator [23,60]:

$$T_\phi^{-1} = \Gamma_\phi = \frac{\gamma}{2} \mathrm{Re}\left[\sqrt{\left(1 + \frac{2i\chi}{\gamma}\right)^2 + \frac{8i\chi}{\gamma} n_{\mathrm{th}}} - 1 \right], \quad (1)$$

where χ is the dispersive coupling, γ is the decay rate of the readout resonator, and $n_{\mathrm{th}} = 1/(e^{hf_R/kT} - 1)$ is the resonator thermal population, set by the fundamental frequency f_r of the resonator. The measured dephasing rate is then given by $T_2^{-1} = T_\phi^{-1} + T_{2,0}^{-1} + 1/(2T_1)$, where T_1 and $T_{2,0}$ are measured by averaging the low-temperature values. The model, which contains only independently

measured quantities, is overlaid for each qubit in Fig. 5(b), showing relatively good agreement. We can also go further by using the measured temperature-dependent values of T_1 to solve for Γ_ϕ directly, as shown in Fig. 5(c), finding that the behavior is well modeled by Eq. (1).

V. CONCLUSIONS

By investigating transmon qubits at higher temperatures and frequencies than before, we gain a new perspective on superconducting-qubit coherence. Our devices highlight the importance of increased frequency, which could even help improve aluminum-microwave-device performance up to approximately 180 mK, relaxing the strict thermalization requirements of current qubits [25,27,42,61], as well as exploring a new regime for studying physics with qubits in a conventional material platform. Beyond this, we have shown that with high-temperature niobium-trilayer Josephson junctions, quasiparticle-based decoherence can be eliminated up to approximately 1 K. Taking advantage of this, we confirm the thermal behavior of qubit dephasing unhindered by relaxation. Above 200 mK, our qubit dephasing begins to see reduction below 1 μs from readout-induced dephasing. Already, these temperatures allow for significantly increased heat dissipation. This enables new opportunities for addressing thermal challenges in quantum processors and new hybrid quantum experiments by reducing experimental complexity. Moreover, expanding the achievable frequencies also expands the range of energy scales that can be modeled with superconducting qubits. Niobium junctions can operate as high as 700 GHz: our devices have only begun to explore this accessible energy range, serving as an important first step

in increasing qubit frequencies and paving the way for even higher-frequency higher-temperature superconducting quantum devices.

APPENDIX A: FABRICATION METHODS

The trilayer junction fabrication process is summarized in Fig. 6. 330 μm-thick C-plane polished sapphire wafers grown with heat-exchange method (HEMEX) are ultrasonically cleaned in toluene, acetone, methanol, isopropanol, and deionized (DI) water, then etched in a piranha solution kept at 40 °C for 2 min and rinsed with deionized water. Immediately following, the wafers are loaded into
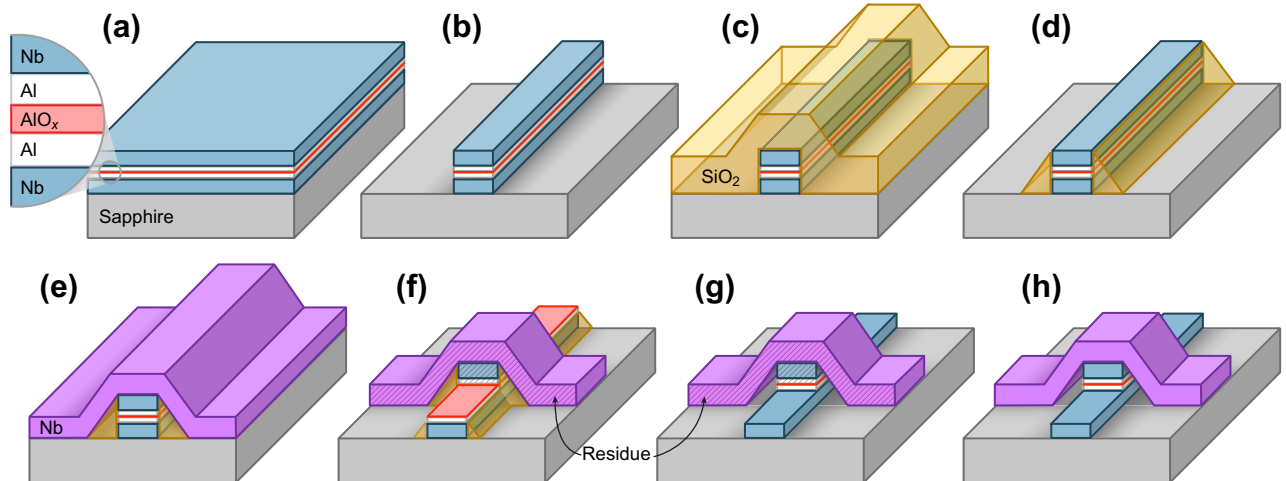
FIG. 6. The junction-fabrication process. (a) The trilayer is deposited and oxidized *in situ*. (b) The first layer is etched with a chlorine reactive ion etch (RIE). (c) The SiO₂ is grown isotropically. (d) The sidewall spacer is formed by anisotropic etching with fluorine chemistry. (e) Surface oxides are cleaned in vacuum and the wiring layer (purple) is deposited. (f) The second junction finger (and other circuit elements) are defined by a fluorine plasma etch that is selective against Al. (g) The final devices undergo a wet etch to further remove SiO₂ and exposed Al (h) Fluorocarbon residues are removed.

a Plassys MEB550S electron-beam evaporation system, where they are baked at $> 200\,^\circ$C under vacuum for 1 h to help remove water and volatiles. When a sufficiently low pressure is reached ($< 5 \times 10^{-8}$ mbar), titanium is electron-beam evaporated to bring the load-lock pressure down even further. The trilayer is now deposited by first evaporating 80 nm of Nb at > 0.5 nm/s while rotating the substrate. After cooling for a few minutes, 8 nm of aluminum is deposited while rotating the substrate at a shallow angle ($10\,^\circ$) to improve conformality. The aluminum is lightly etched with a 400-V 15-mA Ar^+ beam for 10 s, then oxidized with a mixture of 15% O_2 and Ar at a static pressure. After pumping to below ($< 10^{-7}$ mbar), titanium is again used to bring the vacuum pressure down to the low 10^{-8}-mB range. We note that the pressure for the remainder of the trilayer deposition is higher than for the first Nb layer. The second 3-nm layer of Al is evaporated vertically while rotating the substrate to minimize void formation in the following layer. The counterelectrode is then formed by evaporating 150 nm of Nb at > 0.5 nm/s. The substrate is allowed to cool in vacuum for several minutes and we attempt to form a thin protective coating of pure Nb_2O_5 by briefly oxidizing the top surface at 3 mbar for 30 s.

The wafers are mounted on a silicon handle wafer using AZ1518 photoresist cured at $115\,^\circ$C, then coated with 1 µm of AZ MiR 703 photoresist and exposed with a 375-nm laser in a Heidelberg MLA150 direct-write system. The assembly is hardened for etch resistance by a 1-min bake at $115\,^\circ$C, then developed with AZ MIF 300, followed by a rinse in DI water. The entire trilayer structure is now etched in a chlorine inductively coupled plasma–reactive ion etcher (ICP-RIE) (etch 1 in Table I). The plasma conditions are optimized to be in the ballistic ion regime, which gives high etch rates with minimal redeposition. Immediately after exposure to air, the wafer is quenched in DI water: this helps prevent excess lateral aluminum etching by quickly diluting any surface HCl (formed by adsorbed Cl reacting with water vapor in the air). The remaining photoresist is thoroughly dissolved in a mixture of $80\,^\circ$C N-methyl-2-pyrrolidone with a small addition of surfactants, which also removes the substrate from the handle wafer.

The wafer is ultrasonically cleaned with acetone and isopropanol, then SiO_2 spacer is grown with low-temperature

PECVD. SiH_4 and N_2O are reacted in a 100-W plasma with the chamber held at $190\,^\circ$C. The complete process (including chamber cleaning, pumping, and purging steps) takes approximately 15 min. The wafer is then mounted on a silicon handle wafer using Crystalbond 509 adhesive softened at $135\,^\circ$C, then etched in a fluorine reactive ion etch (etch 2 in Table I). This etch is optimized to be directional but in the diffusive regime to promote chemical selectivity while enabling the formation of the spacer structure. At this point, minimizing oxide formation is crucial, since the top surface of the trilayer is exposed and will need to form a good contact to the wiring layer, so immediately following the completion of the etch, wafers are separated from the handle wafer by heating to $135\,^\circ$C, ultrasonically cleaned of remaining adhesive in $40\,^\circ$C acetone and isopropanol, then immediately placed under vacuum in the deposition chamber, where they are gently heated to $50\,^\circ$C for 30 min to remove remaining volatiles.

The contaminated and oxidized top surface of the counter electrode is etched with a 400-V 15-mA Ar^+ beam for 5 min, which is sufficient to remove any residual resistance from the contact. After pumping to below ($< 10^{-7}$ mbar), titanium is used to bring the vacuum pressure down to the low 10^{-8}-mB range. The wiring layer is now formed by evaporating 160 nm of Nb at > 0.5 nm/s. The substrate is allowed to cool in vacuum for several minutes and the wiring layer is briefly oxidized with a mixture of 15% O_2 and Ar at 3 mbar for 30 s to promote a thin protective coating of pure Nb_2O_5. The wafers are again mounted on a handle wafer, coated with AZ MiR 703 photoresist and exposed with a 375-nm laser. The assembly is hardened for etch resistance by a 1-min bake at $115\,^\circ$C before development. The final structure is now defined with a fluorine reactive ion etch (etch 3 in Table I). This step proves to be highly problematic, as it easily forms inert residues and needs to be highly chemically selective in order to avoid etching through the aluminum, so the plasma is operated in a low-density ballistic regime with the addition of O_2, which helps passivate exposed aluminum and increase selectivity. To avoid the formation of excess sulfur silicon residues on the spacer (which we find are even worse than fluorocarbon residues), we reduce the SF_6 content compared to Ref. [33] and increase the Ar content to promote mechanical removal. This instead favors

TABLE I. The plasma-etch parameters used in the inductively coupled plasma–reactive ion etch (ICP-RIE) etches described in the process. The etches are performed in an Apex SLR ICP etcher.

Etch	T ($^\circ$C)	Pressure (mT)	ICP/bias power (W/W)	Cl_2 (sccm)	BCl_3 (sccm)	Ar (sccm)	CF_4 (sccm)	CHF_3 (sccm)	SF_6 (sccm)	O_2 (sccm)	Etch time (s)	Etch rate (nm/s)
1	20 ± 0.1	5	400/50	30	30	10	$\cdots$	$\cdots$	$\cdots$	$\cdots$	50–60	~ 4.5
2	20 ± 0.1	30	500/60	$\cdots$	$\cdots$	10	30	20	$\cdots$	$\cdots$	120–140	~ 2
3	20 ± 0.1	5	400/60	$\cdots$	$\cdots$	10	$\cdots$	40	20	4	65–90	~ 4.5

the formation of fluorocarbon residue, which unlike the silicon residues can later be successfully removed. The etch time is calculated for each wafer based on visual confirmation when the bare wiring layer is etched through. We remove cross-linked polymers from the photoresist surface with a mild 180-W room-temperature oxygen plasma that minimally oxidizes the exposed Nb (though we find that this is not very effective). The remaining resist is now fully dissolved in 80 °C *N*-methyl-2-pyrrolidone with surfactants.

With the junctions now formed, the wafer is ultrasonically cleaned with acetone and isopropanol, coated with a thick protective covering of photoresist (MiR 703) cured at 115 °C, and diced into 7-mm chips. The protective covering is now dissolved in 80 °C *N*-methyl-2-pyrrolidone with surfactants (we find that this can also help to remove stubborn organic residues from previous steps) and the chips are given a final ultrasonic clean with acetone and isopropanol. The remaining silicon spacer is now dissolved by a short (10–15)-s etch in a mixture of ammonium fluoride and acetic acid (AlPAD Etch 639), quenched in deionized water, then carefully dried using isopropanol to preserve the now partially suspended wiring layer. Finally, we remove the aforementioned fluorocarbon residues by etching the chips in a 72 ± 1 °C solution containing hydroxylammine, catechol, and 2-(2-aminoethylamine)-ethanol (Dupont EKC 265). The finished chips are packaged and cooled down within 30 min from this final etch to minimize any NbO_x regrowth from air exposure.

APPENDIX B: FLUOROCARBON REMOVAL METHODS

As mentioned in Appendix A, the carbon and argon content of etch 3 is increased to avoid lossy silicon-spacer residues, which arise in sulfur-rich and carbon-poor plasma-etch chemistries [62]. Unfortunately, this results in more pronounced fluorocarbon residues [33] on finished junctions, as shown in Fig. 7(a). As these residues are comprised of lossy dielectric material, it is essential to remove them to reduce junction loss. To this end, we use commercially available cleaning solution (Dupont EKC 265), specifically optimized to remove organometallic compounds. This alkanolamine solution consists of a polar solvent (H_2O), hydroxylamine, 2-(2-aminoethylamine)-ethanol (AEEA), and catechol [63,64]. The etch mechanism for this mixture begins with the reduction of any organometallic compounds by the hydroxylamine, allowing the compounds to become more soluble in the water and alkanolamine solution [63,64]. This also reduces any exposed metal oxides, which conveniently also removes contaminated surface metal oxides, which are significant sources of loss [36,37].

The catechol, primarily a chelating agent or ligand, allows the now-soluble metal ions to form complexes and avoid precipitating out of solution. The hydroxylamine can also serve as a ligand in solution. Catechol also assists in metal protection and metal-oxide solubilization due to its redox potential between 1.0 V and −2.0 V
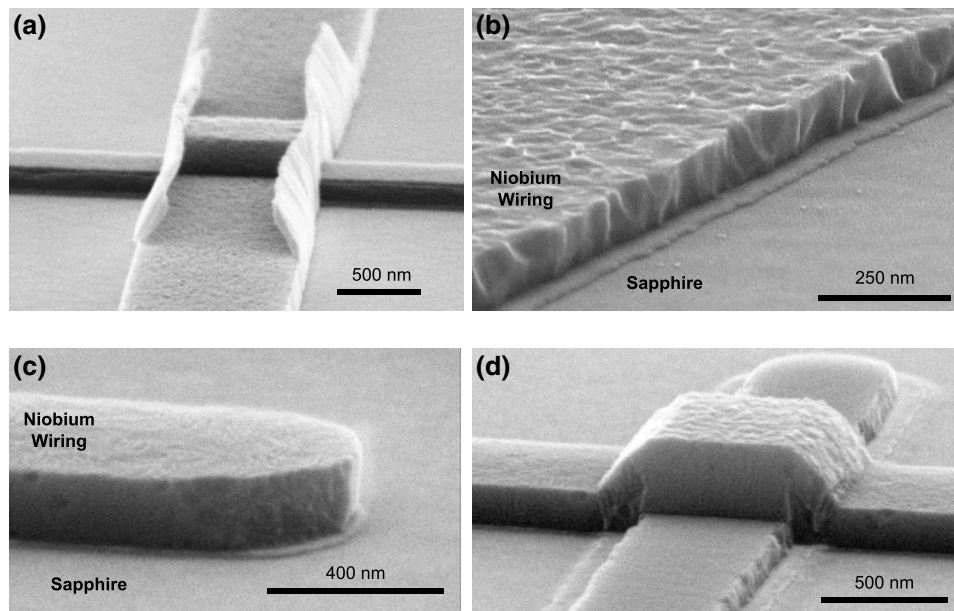

FIG. 7. Fluorocarbon residue removal. (a) With the increased carbon content in etch 3, the untreated finished junctions have fairly pronounced fluorocarbon residues, with minimal spacer residues. (b) The finished junction treated with the EKC mixture (3 min 90 °C EKC) nearly 20° above the target etching temperature shows significant metal attack (about 60 nm). Notably, no signs remain of the fluorocarbon residues on the edges of the Nb wiring layer. (c) When treated between 70 and 75 °C (2 min 72 °C EKC), the metal etch rate is reduced to a reasonable level, while the organometallic residue on the wiring layer is still efficiently removed. This leaves incredibly smooth and virtually residue-free surfaces on all sides of the junction as shown in (d).

(relative to the standard hydrogen electrode) at a pH of 7 [63]. The alkanolamine of choice, AEEA, is an alcohol amine with a relatively high boiling point, a high flash point, and nearly nonexistent metal- or substrate-etch rates under standard process conditions. The two-carbon linkage is key toward reducing the attack on metals and alloyed substrates while enhancing reactivity with organic and organometallic residues. Importantly, this mixture is only moderately acidic, with amines with hydroxyl groups both enhancing solubility and not increasing acidity greatly. Reducing acidity may have the added benefit of reducing surface hydrogen content, which could help limit niobium hydride precipitation at cryogenic temperatures [65], which is known to adversely affect niobium superconducting properties [66] and coherence properties [65].

As shown in Figs. 7(b)–7(d), the mixture is effective at efficiently removing fluorocarbon residue. At the elevated temperatures (approaching the mixture boiling point) shown in Fig. 7(b), the metal etch rate is increased, removing nearly 60 nm of niobium. In practice, this consumes too much of the junction, leaving behind very little of the first niobium layer, and leaves behind ridges, producing a rougher surface. Reducing the etch temperature to 70–75 °C yields much more reasonable etch rates and surface profiles, as shown in Figs. 7(c) and 7(d). Only about 10 nm of niobium is consumed in the process, while the etch demonstrates selectivity toward the organometallic residue materials (which can be up to 30

nm thick). These etch conditions completely remove the fluorocarbon residues and leave a very smooth and lightly etched finish on the junction metal surfaces. Additionally, the mild surface etch ensures lossy surface interfaces and oxides [36,37,50] are removed, which should improve the loss characteristics in the device.

APPENDIX C: HIGH CRITICAL-CURRENT DENSITY WITH PECVD

Realizing qubits above 20 GHz requires Josephson junctions with critical currents higher than 0.1 kA/cm^2. In the self-aligned niobium-trilayer junction-fabrication process [33], this can be achieved by using low-temperature (90 °C) high-density plasma chemical vapor deposition (HDPCVD) when depositing the spacer material, which avoids annealing the junction barrier [67]. Unlike PECVD, which requires hotter deposition temperatures, HDPCVD typically produces more porous material [68]: while the wet-etch rates are faster [68], we empirically find that using HDPCVD spacers leads to worse junction loss properties (This may be a result of the rougher spacer surface producing a lossier metal-spacer interface left behind after the final wet etch.) Since the junction-barrier annealing process is minimal below 200 °C [33,35,67], however, we can use PECVD at reduced temperatures (200–230 °C) while still forming junctions with a relatively high critical-current density. In this way, by limiting the maximum temperatures and the time spent at elevated temperatures,
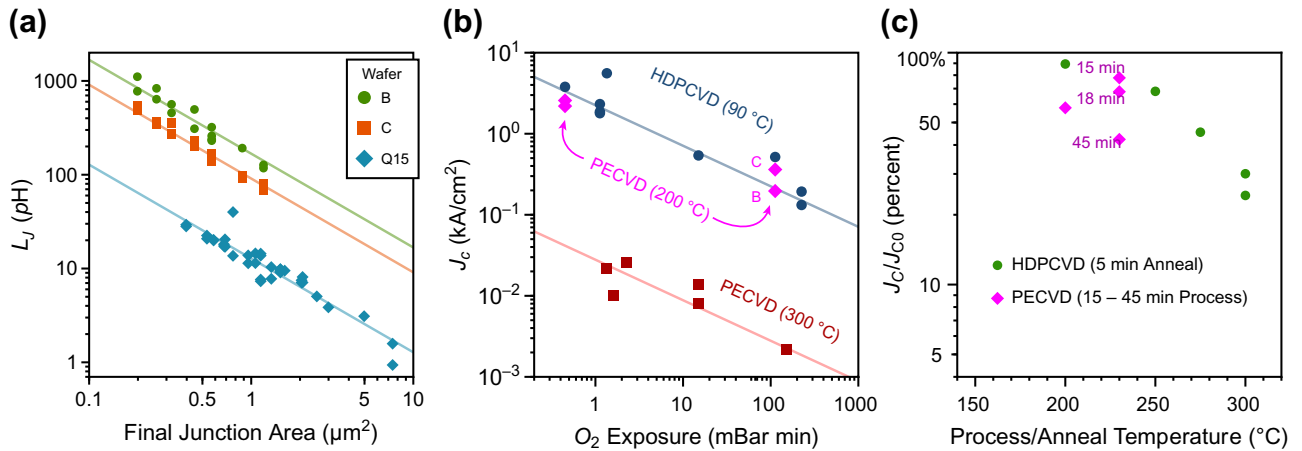

FIG. 8. Low-temperature plasma-enhanced chemical vapor deposition (PECVD) junctions with high J_c. (a) The junction inductance L_J calculated from the normal-junction resistance R_n, measured as a function of the junction area for several different devices with different process conditions, including junctions from wafers B and C (qubits measured in the main text). A linear fit with respect to the junction area yields a measurement of the junction critical-current density J_c. (b) The J_c of niobium-trilayer junctions as a function of the oxygen exposure (red and blue data from Ref. [33]) with the addition of low-temperature PECVD junctions (magenta), which still have a high critical-current density. (c) Reduction of the critical-current density as a function of the anneal temperature, with the addition of the low-temperature PECVD junctions, which are only mildly annealed. The high-density plasma chemical vapor deposition (HDPCVD) junctions (data from Ref. [33]) have been annealed for 5 min, while the junctions that have gone through PECVD have spent more than 15 min at that temperature.

we can replicate the physical spacer properties of the junctions in Refs. [33,35]. This also improves process stability by providing control over a wide range of critical-current densities with a unified process, eliminating the need for switching between PECVD and HDPCVD deposition methods.

Using the relationship between the normal-state resistance R_n and the critical current I_c [69], we can use room-temperature resistance measurements to predict cryogenic junction properties. In Fig. 8(a), we show the Josephson inductance $L_J = \Phi_0/2\pi I_c$ determined from the junction resistance as a function of the final junction area (with lithographic reduction and etch-back taken into account). The solid lines show fits to an inverse function of the area, which can be used to extract the effective critical-current density J_c. Along with test devices containing many junctions with large areas, we also plot witness junctions (with geometries identical to the qubits in the main text) fabricated alongside the qubits, which have different values of J_c resulting from differing process conditions. While the resistance of the qubit junctions is not directly measured, this gives a reasonable estimate of their junction inductance. The junction critical-current density can be easily adjusted by changing the oxygen exposure $E = P_{O_2}T$ (the product of the oxidation time T and the oxygen partial pressure P_{O_2}) during the junction-barrier-formation step [67]. The critical-current densities extracted by fitting the junction resistance are shown as a function of the oxygen exposure E for varying process conditions in Fig. 8(b), overlaid with measurements from Ref. [33]. Our results (magenta) are consistent with the expected $J_c \propto E^{1/2}$ dependence and, importantly, we find that reducing the PECVD deposition temperature from 300 to 200–230 °C results in critical-current densities close to the low-temperature (90 °C) HDPCVD junctions. Going further, we can directly compare the PECVD and HDCPVD processes to estimate the annealing effect of the elevated temperatures. We summarize the reduction in J_c as a function of the PECVD deposition temperature in Fig. 8(c), finding that our process typically maintains more than 50% of the HDPCVD critical-current density. These differences are comparable to the variations in J_c measured from wafer to wafer (likely a result of imperfect process control), so we are not able to resolve a consistent trend with temperature [33,67]. However, comparing the unintentionally different lengths of time each wafer has spent at elevated temperatures [labeled in Fig. 8(c)] could help to explain the J_c variations. Automating and further refining the fabrication process described in Appendix A may help further increase the junction consistency. Nevertheless, within a practically accessible oxygen exposure, our junction process can realize critical-current densities between 100 A/cm^2 and 2.5 kA/cm^2, while also taking advantage of the smoother and more conformal PECVD spacer surface.

APPENDIX D: LOW-LOSS K-BAND PACKAGING

Chips with several qubits and their readout resonators sharing a common microwave feed line are mounted in a K-band [(18–27)-GHz] package shown in Fig. 9, which is carefully engineered for low-loss operation from dc to 30 GHz. Inspired by microwave solutions [70], the package aims to shield the qubits from decoherence from external fields and thermalize the sapphire chip containing the qubits, while adding minimal unwanted resonant modes and efficiently routing signals to and from the chip with minimal dissipation and reflection. We accomplish this with a copper-clad porous ceramic filled polytetrafluoroethylene (PTFE) dielectric (Rogers 3003) circuit board, patterned with via-fenced [71] coplanar waveguides for signal routing. The sapphire substrate is clamped to the circuit board by a high-purity copper enclosure, as shown in Fig. 9(b). This enclosure is composed of three precision-machined pieces, which thermalize and mechanically secure the sample and prevent leakage by fully enclosing the chip on all sides. To minimize potential damage to the delicate surface of the chip from accidents during mounting, the chip is first placed into a slot on the copper anvil piece, where it sits on short sections of soft indium wire located on each corner. The enclosure is designed to naturally align patterns on the chip surface with the circuit board: as the anvil is screwed into the copper base, the anvil geometry aligns the chip within a tolerance of 0.005 in. and the indium wire deforms into the machined pocket, firmly securing the sapphire. When assembled, the sapphire substrate is suspended so that the surface qubits are well separated from the lossy copper surfaces [70], with the resulting dimensions optimized such that the nearest package mode lies above 27 GHz. To further minimize potential loss contributions from the copper, the anvil and lid are polished and the copper oxide is etched with glutamic acid (flux) immediately prior to packaging. Further improvement could be achieved by plating the copper surface [70].

The signal is coupled on and off the sapphire substrate with wire bonds. Since each of these has a high inherent inductance of about 1 nH/mm [72], which is increasingly problematic at higher frequencies, we use sets of three wire bonds for each connection. Using finite-element-method simulations (ANSYS HFSS), we simulate and optimize the wire-bond location and profile in conjunction with the on-chip signal-launch geometry for best performance in the K band. The final geometry is illustrated in Fig. 10(a). To estimate the package performance and avoid unwanted resonant modes in lengths of transmission line, we also simulate the scattering parameters of the entire package, which includes the entire chip and circuit board. The simulated parameters, shown in Fig. 10(b), suggest an insertion loss better than 0.2 dB up to 27 GHz, after which the
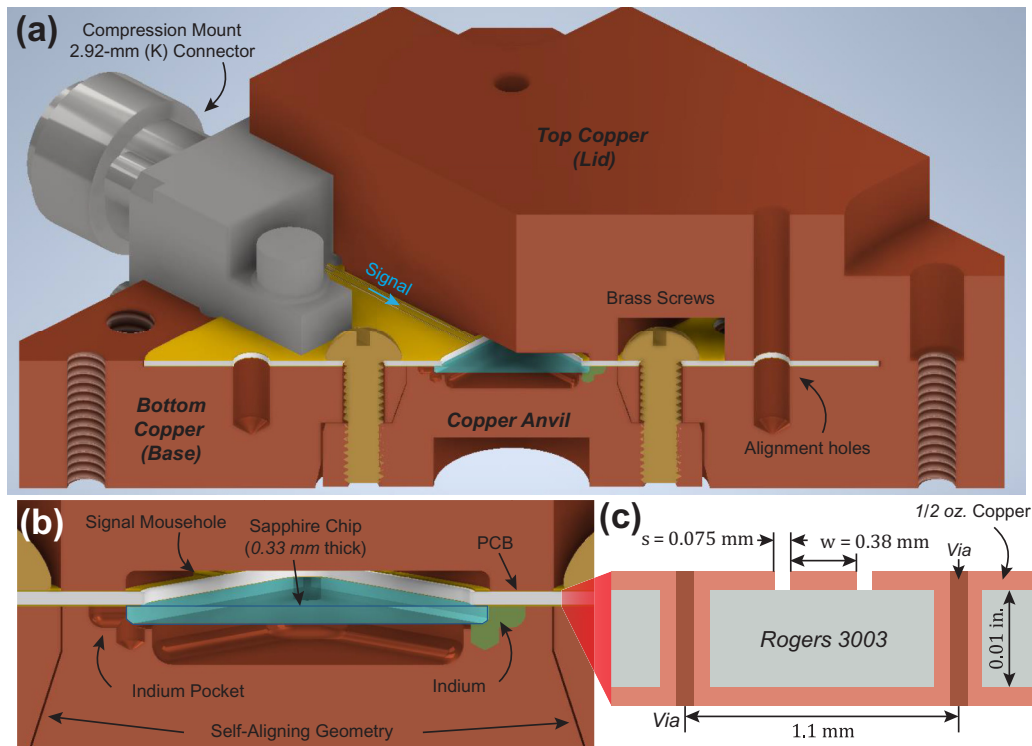
FIG. 9. (a) Cutaway renderings of the K-band packaging, highlighting the three machined copper pieces that secure, thermalize, and electrically shield devices patterned on the sapphire chip (blue). (b) A close-up view shows how the sapphire chip is held in the anvil piece with sections of indium wire: as the anvil is screwed into the base, the anvil geometry aligns the chip within a tolerance of 0.005 in. and the indium wire (green) deforms into the machined pocket, firmly securing the sapphire. (c) The package also routs a signal from K connectors to and from on-chip devices. This is accomplished with a circuit board fabricated using a low dielectric constant substrate with good high-frequency loss properties. Plated vias on either side of the signal trace combined with a mousehole slot in the copper lid ensure that the signal is confined without excessive leakage and unwanted resonances.

impedance-mismatch effects become increasingly pronounced. While not visible in Fig. 10(b), the simulations also suggest the presence of weakly coupled modes localized in the substrate and indium mounting regions, typically between 25 and 29 GHz (depending on the exact geometry of the deformed indium). Combined with reduced transmission at higher frequencies, this determines an upper useful operating range of about 27 GHz for this packaging design.

APPENDIX E: CRYOGENIC MEASUREMENT SETUP

The K-band package described in Appendix D is thermalized to the base stage of an Oxford Triton 200 dilution refrigerator (lowest mixing-chamber temperature 65–95 mK), where transmission measurements through the central feed line can be used to characterize resonators and qubits. The mounted assembly is encased in two layers of Mu-metal magnetic shielding to reduce decoherence from stray magnetic fields, as shown in Fig. 11. The qubits

are also protected from noise coming from the input line by 50 dB of cryogenic attenuation: these cryogenic attenuators maintain their properties up to excessively high frequencies (65 GHz), which helps to ensure that the noise temperature reaching the qubits is sufficiently low, even for higher-frequency harmonics, which will also be properly attenuated. After passing through the sample, two cryogenic isolators along with a superconducting Nb-Ti cable minimize signal dissipation while continuing to shield the qubits from thermal radiation. A cryogenic low-noise amplifier (noise temperature around 8.5 K) combined with a low-noise room-temperature amplifier help to increase the output signal power to easily measurable levels while maintaining a good signal-to-noise ratio.

The resonators and qubit transitions are characterized with continuous-wave single- and two-tone spectroscopy, using a Agilent E5071C network analyzer (not shown in Fig. 11). For pulsed qubit measurements, we use a Quantum Instrument Control Kit [73] based on the Xilinx RFSoC ZCU111 field-programmable gate array (FPGA) to synthesize and measure pulses, which are up- and
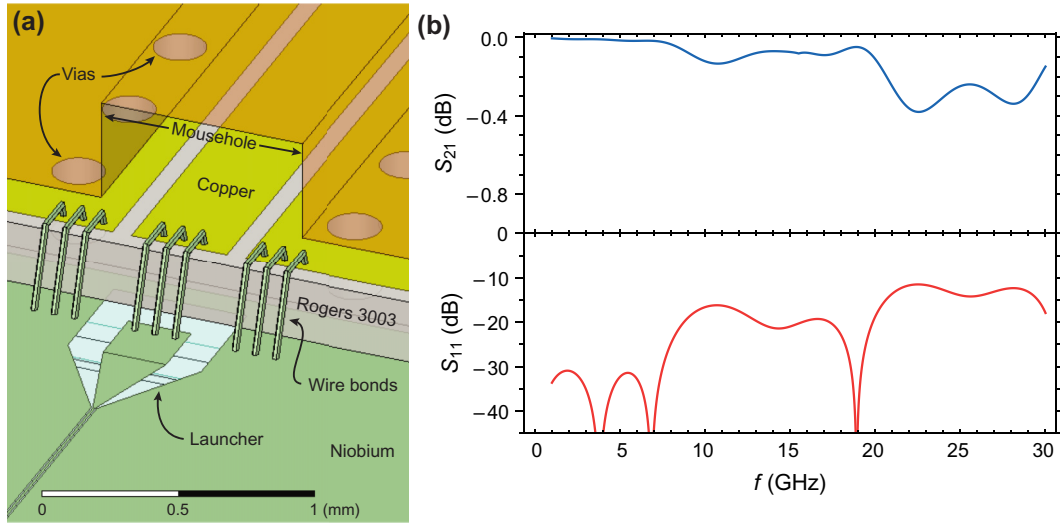
FIG. 10. (a) The optimized launcher geometry and wire-bond configuration, which achieves maximal transmission up to 27 GHz. Using a manual wire bonder, we attempt to replicate this wire-bond shape; however, in practice, the circuit-board dimensions require slightly longer bonds. (b) The simulated transmission and reflection through the K-band package containing a chip with a straight transmission line connected to the optimized launch and wire-bond geometry. Not taking into account metal dissipation and insertion loss from the circuit-board connectors, the simulations predict a total insertion loss better than 0.2 dB up to 27 GHz for each transition.

down-converted with the heterodyne measurement setup shown in Fig. 11. The FPGA and carrier-signal generators are clocked to a 10-MHz rubidium source for frequency stability. Although the frequencies used can technically be sent through SMA connectors, in practice working at the edge of the connector operating band causes increased issues with impedance mismatches and unwanted circuit modes. Since many components used in the setup are designed to operate at higher frequencies, we primarily use 2.92-mm (K) connectors for routing signals. Since the individual filters (marked with stars in Fig. 11) have fairly wide bandwidths, we adjust the filter network to best match the frequency of each individual qubit, in order to maximize transmission at the qubit frequencies while filtering out leaking local oscillator signals and unwanted images.

APPENDIX F: RABI OSCILLATIONS WITH FINITE PULSES

An applied signal on resonance with f_{ge} will result in Rabi oscillations between the ground and excited states at a Rabi frequency Ω proportional to the signal amplitude. In the main text, we explore this behavior by applying fixed-length Gaussian pulses near the qubit frequency, which have the following pulse envelope function:

$$\Omega(t) = \Omega_0 \exp\left[-\frac{t^2}{2\sigma^2}\right], \quad -n\sigma < t < n\sigma. \quad \text{(F1)}$$

For practical purposes, the pulse length is finite, which is achieved by truncating the Gaussian envelope at $\pm n\sigma$. For

simplicity, the resolution of the stored pulse wave form is limited to the FPGA processor speed, so we instead explore Rabi oscillations by varying the pulse amplitude (over which we have much finer control). This behavior is sinusoidal and results in periodic fringes with the qubit in its excited state, as shown in Fig. 2(b). For a continuous signal detuned from the qubit transition by Δ, the excited-state probability of the qubit would be given by [45]

$$P_e(t) = \frac{\Omega^2}{\Omega^2 + \Delta^2} \sin^2(\pi\Omega t). \quad \text{(F2)}$$

The finite Gaussian nature of the pulse that we use complicates the qubit evolution, however, since the Rabi evolution rate is nonuniform during the pulse [44] and the truncated pulse edges introduce nonadiabaticity in the qubit-state evolution [43]. For a truncated Gaussian pulse as described in Eq. (F2), the excited-state population can be modeled by [44,45]

$$P_e = \frac{\Omega^2 e^{-n^2}}{\Omega^2 e^{-n^2} + \Delta^2} \sin^2\left(\frac{\sigma}{2}\int_{-n}^{n}\partial\tau\sqrt{\Omega^2 e^{-\tau^2} + \Delta^2}\right). \quad \text{(F3)}$$

On resonance ($\Delta = 0$), we recover the familiar expression $P_e = \sin^2(\pi\sigma\Omega)$. However, off resonance, the expected power broadening of the Rabi oscillations in frequency space is reduced, as shown in Fig. 12. For small n, the behavior is similar to that of a square pulse [45]; however,
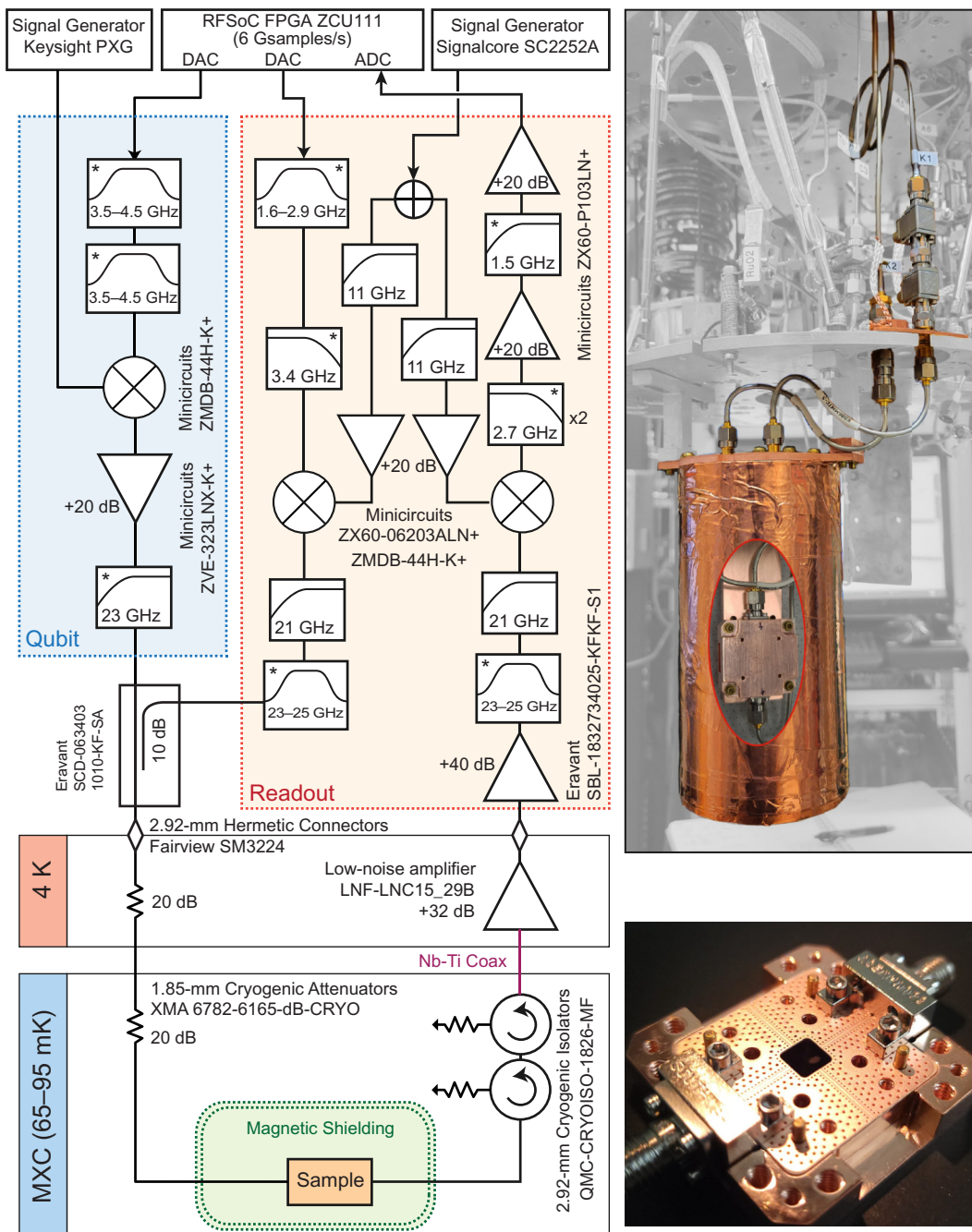
FIG. 11.   A schematic of the high-frequency microwave-measurement setup used for qubit characterization. The colored tabs show the temperature stages inside the dilution refrigerator. A composite photograph (top right) highlights the relevant hardware in the dilution refrigerator, with a cutaway showing the location of the copper sample box inside the magnetic shield. A photograph (bottom right) shows the sample box with the top and anvil copper pieces removed.

as we include more of the Gaussian profile by increasing the cutoff length n, the bandwidth of the oscillations decreases while the frequency scaling of the oscillations remains constant. While this model neglects bandwidth effects on the pulse envelope reaching the qubit, the behavior shown in Fig. 12 qualitatively matches the behavior observed in Fig. 2(b).

APPENDIX G: TIME DEPENDENCE OF COHERENCE

The qubit coherence is expected to fluctuate in time, both from lossy coupled two-level systems [47–49] as well as nonequilibrium quasiparticles that can be generated by high-energy particle impacts [27,74–77]. To investigate this, we measure the coherence properties of a qubit as a
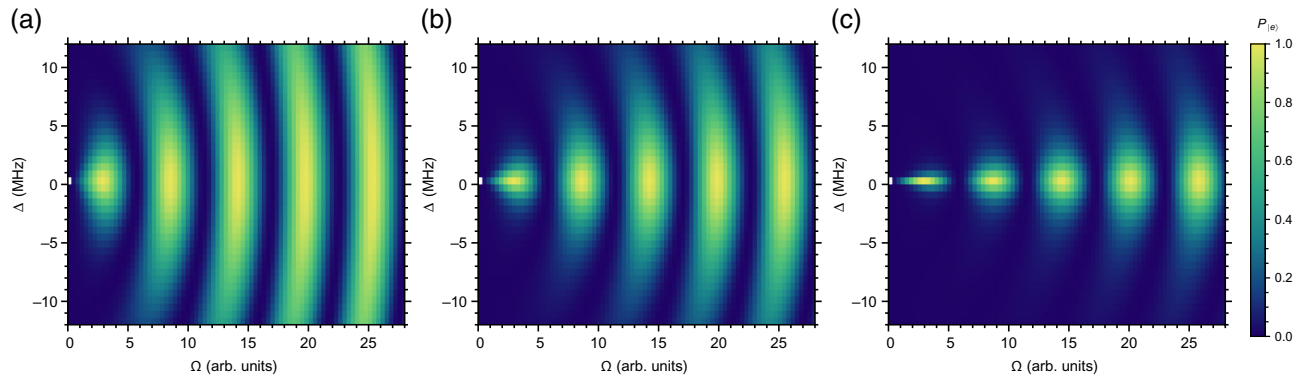
FIG. 12.   The excited-state population following a finite-length Gaussian pulse terminated at $\pm n\sigma$, shown for different values of n: (a) $n = 1.5$; (b) $n = 2.0$; (c) $n = 2.5$. For smaller n, the pulse shape is closer to a square pulse and the fringes exhibit significant power broadening. As more of the Gaussian envelope is used, the fringe bandwidth is reduced, limiting the power-broadening effect. Here, the pulse lengths σ have been adjusted to yield similar oscillation rates at $\Delta = 0$.

function of time, as shown in Fig. 13(a). We interleave faster and slower experiments with 1000 and 3×10^5 averages, respectively, each of which has a different fit uncertainty σ_m. After propagating out the respective average fit uncertainty $\langle \sigma_m \rangle$, we estimate that the qubit coherence fluctuation can be described by a Gaussian probability distribution with $\sigma_{T1} = 6 \pm 1\%$ of the qubit T_1. To speed up measurements, these population-decay experiments are each performed with fewer than ten delay points; however, many averages are still needed to estimate the population decay rate. Combined with data-transfer times, the shortest experiment spacing achieved in Fig. 13(a) is around 3 s, which is sufficient to capture slow effects such as two-level system (TLS) population fluctuations [47–49].

Other dissipation processes such as quasiparticle relaxation [25,26,38] occur on a much faster time scale, especially in niobium [31]. Since our devices are firmly in the transmon limit [39], we cannot leverage charge sensitivity to monitor quasiparticle dissipation dynamics through discrete charge fluctuations [74]. To explore decoherence events with higher time resolution, we turn to rapid qubit error measurements similar to those of Refs. [75,76]. Our measurement protocol [illustrated in Fig. 13(b)] consists of a deconstructed population-decay experiment, in which the qubit is excited and then measured following a short delay $\tau = 260$ ns. We wait for several coherence lengths (4 μs) in between experiments to ensure that the qubit cools back down to its ground state. The qubit state is measured (with readout fidelity 60%) and we count the percentage of errors occurring in a window of fixed time. We note that due to hardware bandwidth limitations, we are only able to measure a single qubit at a time, which limits the information gained by this measurement.

The error rates are summarized as a function of time using increasing window lengths in Fig. 13(c). Since we are measuring single-qubit errors and not correlated qubit errors [75,76], our measurements cannot differentiate

between different types of errors. As a result, the time-series data in Fig. 13(c) are dominated by a combination of readout errors and qubit errors from population decay. An event generating an aluminum quasiparticle is expected to produce significant sustained increases in single and correlated qubit errors over durations of milliseconds [75–77]. Other than small fluctuations [not inconsistent with T_1 distributions found in Fig. 13(a)], we do not observe conclusive signs of such millisecond-scale events. As niobium quasiparticles are expected to have lower equilibrium densities and much faster recombination rates on the order of 5 ns [31], we cannot conclusively confirm or deny the presence or frequency of nonequilibrium quasiparticle events in our qubits. However when combined with the thermal dependence of coherence properties, we believe that the absence of consistent qubit errors on millisecond time scales may suggest that our loss channels are primarily dominated by nonquasiparticle sources.

APPENDIX H: QUBIT THERMAL PERFORMANCE IN CONTEXT

Our qubits benefit from both higher frequencies as well as a higher-energy-gap superconductor, which increases the temperatures at which quasiparticle effects are observed. As a comparison, it is useful to place their performance in context with a conventional microwave qubit: in Fig. 14, we show the measured relaxation and dephasing times of a standard aluminum-junction microwave qubit (the same device compared to the one used in Ref. [33]) plotted alongside the devices discussed in the main text.

The qubit relaxation times are determined by qubit heating from its environment, which depends on the qubit frequency and environment temperature [59], a low-temperature loss limit $T_{1,0}$ determined by independent sources of dissipation, as well as quasiparticle tunneling
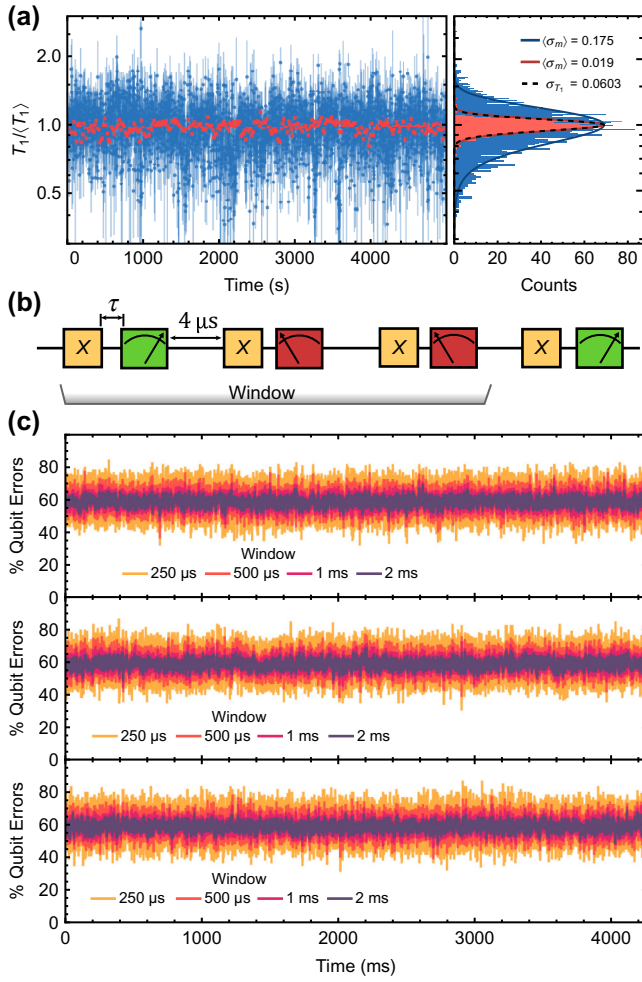
FIG. 13. Temporal measurements with qubit C1. (a) The decoherence time T_1 measured as a function of time, with low- (blue) and higher-average-number experiments (red) interleaved. Taking into account the individual fit errors, a cumulative histogram for both suggests that qubit T_1 has a variance of about 6%. (b) Rapid qubit error measurements are made by applying a π pulse and then measuring the qubit after a short delay τ. The experiments are repeated after a relaxation delay of 4 μs and the percentage of qubit errors is counted in a moving time window. (c) Several time-dependent qubit error measurements with 10^6 points, taken at different times, each shown with varying time-window lengths. Here, the measurement is performed with a delay of $\tau = 260$ ns, so a significant error baseline is observed from T_1 decay and limited readout fidelity. We observe fluctuations consistent with small variations in T_1. These measurements do not reveal conclusive signs of sustained qubit errors on a millisecond time scale, such as those observed during cosmic ray events.

loss T_{qp} [28,29], resulting in the following model for temperature dependence:

$$\frac{1}{T_1(T)} = \frac{1 + \coth\left(\frac{\hbar\omega_q}{2kT}\right)}{T_{1,0}} + \frac{1}{T_{qp}(T)}. \tag{H1}$$

Here, the quasiparticle tunneling loss can be approximated as a function of the temperature, the qubit frequency ω_q, and the superconducting energy gap of the junction Δ, using Bessel functions K_0 and K_1 as follows [28,29,78]:

$$T_{qp} \simeq \frac{4\omega_q}{\pi} e^{-\Delta/kT} \cosh\left[\frac{\hbar\omega_q}{2kT}\right]$$
$$\times \left(K_0\left[\frac{\hbar\omega_q}{2kT}\right] + \frac{\hbar\omega}{4\Delta} K_1\left[\frac{\hbar\omega}{2kT}\right] \right). \tag{H2}$$

We find that this model is fairly accurate for describing qubit relaxation times for both niobium- and aluminum-junction qubits, as shown in Fig. 14. As expected, the relaxation times of the aluminum junction qubit drop rapidly around 160 mK as the quasiparticle decoherence term becomes dominant. From Eq. (H2), we observe that the niobium-junction qubit would begin to see impacts from quasiparticle-tunneling contributions only above approximately 1.1 K.

Unlike the relaxation time, the qubit dephasing times largely depend on the readout-resonator properties. As described in the main text, the dephasing time has contributions from relaxation, along with pure dephasing from both the readout resonator and the environment:

$$\frac{1}{T_2} = \frac{1}{T_\phi} + \frac{1}{T_{2,0}} + \frac{1}{2T_1}. \tag{H3}$$

For the devices in the main text, the relaxation time is fairly constant, so we primarily observe the effects of pure dephasing. However, for the aluminum qubit, shown in Fig. 14(b), we observe three regimes in which the qubit is first dominated by fairly constant dephasing from the environment, then reduced by contributions from the readout resonator above approximately 50 mK, and finally, above approximately 150 mK, is rapidly reduced by the drop in relaxation time caused by quasiparticle tunneling. At the highest temperatures measured, the microwave qubit is sensitive to the line width of the readout resonator, which is in turn also likely increasing due to quasiparticle loss [30] (which explains the deviations, as we do not include this effect in the model). As a result of the significant frequency difference, the aluminum-qubit dephasing is comparable to the K-band qubits at approximately 140 mK.

This model of the thermal dependence of relaxation and dephasing leads to some interesting conclusions for qubit design. Consider a hypothetical microwave qubit with improved performance ($T_{1,0} = T_{2,0} = 150$ μs) and, otherwise, frequencies and properties identical to those of the measured microwave device (magenta). Plotting this performance with dashed cyan lines in Figs. 14(a) and 14(b), we observe that the relaxation time behaves similarly to the measured device, with a sharp drop from quasiparticle tunneling around 150 mK, while the dephasing times begin to decrease at temperatures as
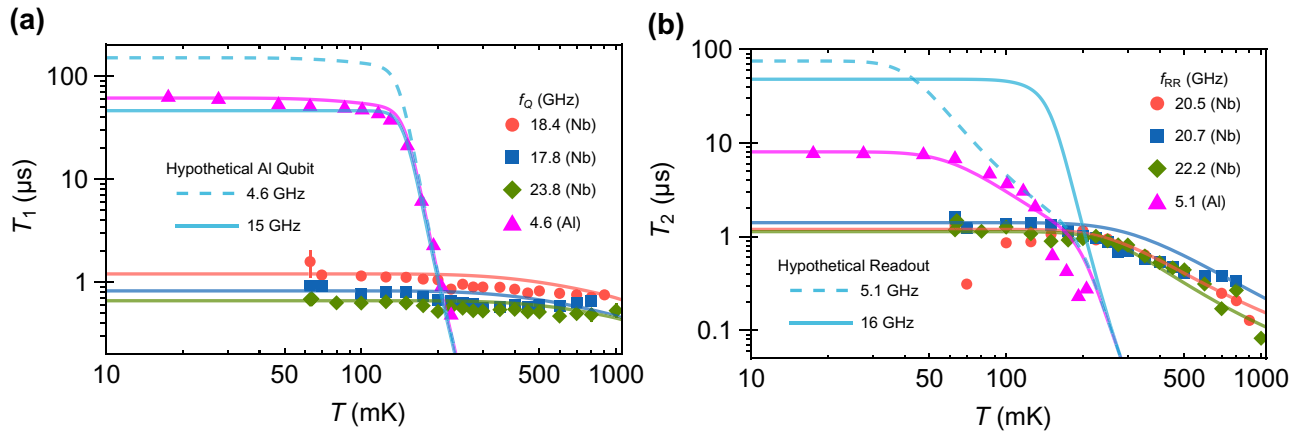
FIG. 14.   (a) The relaxation time for the K-band niobium qubits from the main text (labeled with the qubit frequency) along with a microwave aluminum qubit [33] (magenta), which showcases a much sharper drop in T_1 around 160 mK. Hypothetical aluminum-junction qubits with better performance are shown in cyan: we assume a fixed quality factor Q_1, which results in different base-temperature relaxation times; however, the thermal dependence is unchanged. (b) The dephasing time for the K-band and microwave qubits. In addition to the limitations of quasiparticle effects above 160 mK, the microwave-qubit performance is degraded by excess thermal population in its readout resonator: this effect remains even if low-temperature performance is improved (dashed cyan). This dephasing can be mitigated by increasing the readout-resonator frequency (solid cyan).

low as 50 mK. Now consider the same hypothetical aluminum qubit but scaled up approximately threefold in frequency, shown with a solid line. Assuming that the relaxation loss has material origins, the qubit quality factor will remain constant: this leads to an inverse reduction in the relaxation time, with the thermal dependence largely unchanged. Examining the thermal dependence of the dephasing, however, we conclude that an aluminum qubit merely 3 times higher in frequency should yield

significant performance improvements between 100 and 200 mK. Operating beyond these temperatures requires also addressing the quasiparticle loss through the use of a higher-energy-gap junction, as done with the qubits in the main text.

Evidently, increased frequency can be a powerful tool for improving qubit performance at higher temperatures. For the 20-GHz qubits described in the main text, we observe limits to the dephasing performance above
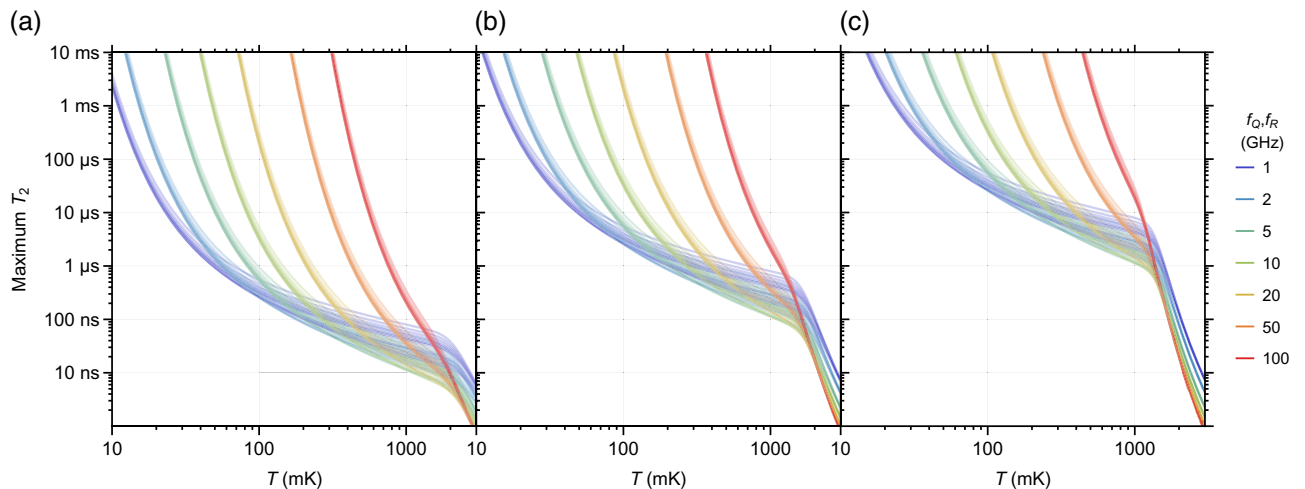

FIG. 15.   Maximum dephasing for all-niobium qubits, considering only thermal dephasing from the readout resonator and relaxation from quasiparticle tunneling: (a) readout-resonator $Q = 10^3$; (b) readout-resonator $Q = 10^4$; (c) readout-resonator $Q = 10^5$. For a better comparison between frequencies, the readout-resonator line width γ is determined by the unitless quality factor $Q = \omega_R/\gamma$ and dispersive shifts χ between 0.3γ and 5γ are considered. From this model, an increase in qubit and readout-resonator frequency will result in improved dephasing times, particularly at lower temperatures. Higher frequencies also increase the maximum operating temperature, with frequencies on the order of 100 GHz increasing the dephasing performance near temperatures of 1 K.

approximately 250 mK. Similar to the hypothetical example discussed above, however, a further threefold increase in the niobium-qubit frequency to 60–75 GHz could eliminate this thermal sensitivity and enable good performance at temperatures up to 1 K. To illustrate this, we consider the maximum-possible dephasing times for a niobium-junction qubit in Fig. 15, where we assume a perfect device with $T_{1,0} = T_{2,0} = \infty$. For any qubit design, quasiparticle-induced decoherence becomes dominant above approximately 1.1 K. The low-temperature dephasing performance is sensitive to qubit parameters, however, and can be improved by decoupling the qubit from its readout resonator: achieved by either increasing the readout-resonator quality factor $Q = \omega_R/\gamma$ or, to a lesser extent, by reducing the dispersive shift χ. However, since this also reduces the state-measurement fidelity, this approach is less practical.

On the other hand, increasing the readout-resonator frequency for a given qubit design leads to dramatic improvements, particularly for lower temperatures. From Fig. 15, we also observe that as frequencies increase, so too does the maximum operating temperature (above which dephasing times decrease below a particular threshold). From this we conclude that increasing the frequency of our K-band qubits to millimeter-wave frequencies (near 100 GHz) could further extend their operating temperatures from 250 mK to 1 K.

---

[1] A. Clerk, K. Lehnert, P. Bertet, J. Petta, and Y. Nakamura, Hybrid quantum systems with circuit quantum electrodynamics, Nat. Phys. **16**, 257 (2020).

[2] Z.-L. Xiang, S. Ashhab, J. Q. You, and F. Nori, Hybrid quantum circuits: Superconducting circuits interacting with other quantum systems, Rev. Mod. Phys. **85**, 623 (2013).

[3] M. Kjaergaard, M. E. Schwartz, J. Braumüller, P. Krantz, J. I.-J. Wang, S. Gustavsson, and W. D. Oliver, Superconducting qubits: Current state of play, Annu. Rev. Condens. Matter Phys. **11**, 369 (2020).

[4] F. Pobell, *Matter and Methods at Low Temperatures* (Springer-Verlag, Berlin, 2007).

[5] M. Pechal and A. H. Safavi-Naeini, Millimeter-wave interconnects for microwave-frequency quantum machines, Phys. Rev. A **96**, 042305 (2017).

[6] P. Magnard, S. Storz, P. Kurpiers, J. Schär, F. Marxer, J. Lütolf, T. Walter, J.-C. Besse, M. Gabureac, K. Reuer, *et al.*, Microwave quantum link between superconducting circuits housed in spatially separated cryogenic systems, Phys. Rev. Lett. **125**, 260502 (2020).

[7] C.-H. Liu, A. Ballard, D. Olaya, D. R. Schmidt, J. Biesecker, T. Lucas, J. Ullom, S. Patel, O. Rafferty, A. Opremcak, *et al.*, Single flux quantum-based digital control of superconducting qubits in a multi-chip module, PRX Quantum **4**, 030310 (2023).

[8] E. Leonard Jr, M. A. Beck, J. Nelson, B. G. Christensen, T. Thorbeck, C. Howington, A. Opremcak, I. V. Pechenezhskiy, K. Dodge, N. P. Dupuis, *et al.*, Digital coherent control of a superconducting qubit, Phys. Rev. Appl. **11**, 014009 (2019).

[9] R. McDermott and M. Vavilov, Accurate qubit control with single flux quantum pulses, Phys. Rev. Appl. **2**, 014007 (2014).

[10] S. Krinner, S. Storz, P. Kurpiers, P. Magnard, J. Heinsoo, R. Keller, J. Lütolf, C. Eichler, and A. Wallraff, Engineering cryogenic setups for 100-qubit scale superconducting circuit systems, EPJ Quantum Technol. **6**, 1 (2019).

[11] Y. Wu, *et al.*, Strong quantum computational advantage using a superconducting quantum processor, Phys. Rev. Lett. **127**, 180501 (2021).

[12] F. Arute, *et al.*, Quantum supremacy using a programmable superconducting processor, Nature **574**, 505 (2019).

[13] Y. Kim, A. Eddins, S. Anand, K. X. Wei, E. van den Berg, S. Rosenblatt, H. Nayfeh, Y. Wu, M. Zaletel, K. Temme, and A. Kandala, Evidence for the utility of quantum computing before fault tolerance, Nature **618**, 500 (2023).

[14] A. Kumar, A. Suleymanzade, M. Stone, L. Taneja, A. Anferov, D. I. Schuster, and J. Simon, Quantum-enabled millimetre wave to optical transduction using neutral atoms, Nature **615**, 614 (2023).

[15] C. Wang, I. Gonin, A. Grassellino, S. Kazakov, A. Romanenko, V. P. Yakovlev, and S. Zorzetti, High-efficiency microwave-optical quantum transduction based on a cavity electro-optic superconducting system with long coherence time, npj Quantum Inf. **8**, 149 (2022).

[16] M. Mirhosseini, A. Sipahigil, M. Kalaee, and O. Painter, Superconducting qubit to optical photon transduction, Nature **588**, 599 (2020).

[17] W. Jiang, C. J. Sarabalis, Y. D. Dahmani, R. N. Patel, F. M. Mayor, T. P. McKenna, R. Van Laer, and A. H. Safavi-Naeini, Efficient bidirectional piezo-optomechanical transduction between microwave and optical frequency, Nat. Commun. **11**, 1166 (2020).

[18] L.-C. Han, Y. Xu, J. Lin, F.-S. Chen, S.-W. Li, C. Guo, N. Li, D.-D. Li, Y.-H. Li, M. Gong, *et al.*, Active reset of superconducting qubits using the electronics based on rf switches, AIP Adv. **13**, 095206 (2023).

[19] P. Magnard, P. Kurpiers, B. Royer, T. Walter, J.-C. Besse, S. Gasparinetti, M. Pechal, J. Heinsoo, S. Storz, A. Blais, and A. Wallraff, Fast and unconditional all-microwave reset of a superconducting qubit, Phys. Rev. Lett. **121**, 060502 (2018).

[20] Z. Wang, M. Xu, X. Han, W. Fu, S. Puri, S. M. Girvin, H. X. Tang, S. Shankar, and M. H. Devoret, Quantum microwave radiometry with a superconducting qubit, Phys. Rev. Lett. **126**, 180501 (2021).

[21] S. O. Valenzuela, W. D. Oliver, D. M. Berns, K. K. Berggren, L. S. Levitov, and T. P. Orlando, Microwave-induced cooling of a superconducting qubit, Science **314**, 1589 (2006).

[22] Z. Wang, S. Shankar, Z. K. Minev, P. Campagne-Ibarcq, A. Narla, and M. H. Devoret, Cavity attenuators for superconducting qubits, Phys. Rev. Appl. **11**, 014031 (2019).

[23] A. A. Clerk and D. W. Utami, Using a qubit to measure photon-number statistics of a driven thermal oscillator, Phys. Rev. A **75**, 042302 (2007).

[24] R. McDermott, Materials origins of decoherence in superconducting qubits, IEEE Trans. Appl. Supercond. **19**, 2 (2009).

[25] T. Connolly, P. D. Kurilovich, S. Diamond, H. Nho, C. G. Bøttcher, L. I. Glazman, V. Fatemi, and M. H. Devoret, Coexistence of nonequilibrium density and equilibrium energy distribution of quasiparticles in a superconducting qubit, Phys. Rev. Lett. **132**, 217001 (2024).

[26] J. M. Martinis, M. Ansmann, and J. Aumentado, Energy decay in superconducting Josephson-junction qubits from nonequilibrium quasiparticle excitations, Phys. Rev. Lett. **103**, 097002 (2009).

[27] K. Serniak, M. Hays, G. de Lange, S. Diamond, S. Shankar, L. D. Burkhart, L. Frunzio, M. Houzet, and M. H. Devoret, Hot nonequilibrium quasiparticles in transmon qubits, Phys. Rev. Lett. **121**, 157701 (2018).

[28] G. Catelani, R. J. Schoelkopf, M. H. Devoret, and L. I. Glazman, Relaxation and frequency shifts induced by quasiparticles in superconducting qubits, Phys. Rev. B **84**, 064517 (2011).

[29] G. Catelani, Parity switching and decoherence by quasiparticles in single-junction transmons, Phys. Rev. B **89**, 094522 (2014).

[30] D. C. Mattis and J. Bardeen, Theory of the anomalous skin effect in normal and superconducting metals, Phys. Rev. **111**, 412 (1958).

[31] A. Leo, G. Grimaldi, R. Citro, A. Nigro, S. Pace, and R. Huebener, Quasiparticle scattering time in niobium superconducting films, Phys. Rev. B **84**, 014536 (2011).

[32] S. Kim, H. Terai, T. Yamashita, W. Qiu, T. Fuse, F. Yoshihara, S. Ashhab, K. Inomata, and K. Semba, Enhanced coherence of all-nitride superconducting qubits epitaxially grown on silicon substrate, Commun. Mater. **2**, 1 (2021).

[33] A. Anferov, K.-H. Lee, F. Zhao, J. Simon, and D. I. Schuster, Improved coherence in optically-defined niobium trilayer junction qubits, Phys. Rev. Appl. **21**, 024047 (2024).

[34] B. W. Petley, The Josephson effects, Contemp. Phys. **10**, 139 (1969).

[35] L. Grönberg, M. Kiviranta, V. Vesterinen, J. Lehtinen, S. Simbierowicz, J. Luomahaara, M. Prunnila, and J. Hassel, Side-wall spacer passivated sub-μm Josephson junction fabrication process, Supercond. Sci. Technol. **30**, 125016 (2017).

[36] J. Verjauw, A. Potočnik, M. Mongillo, R. Acharya, F. Mohiyaddin, G. Simion, A. Pacco, T. Ivanov, D. Wan, A. Vanleenhove, *et al.*, Investigation of microwave loss induced by oxide regrowth in high-Q niobium resonators, Phys. Rev. Appl. **16**, 014018 (2021).

[37] A. Premkumar, C. Weiland, S. Hwang, B. Jäck, A. P. Place, I. Waluyo, A. Hunt, V. Bisogni, J. Pelliciari, A. Barbour, *et al.*, Microscopic relaxation channels in materials for superconducting qubits, Commun. Mater. **2**, 1 (2021).

[38] K. Serniak, Ph.D. thesis, Yale University, 2019.

[39] J. Koch, M. Y. Terri, J. Gambetta, A. A. Houck, D. I. Schuster, J. Majer, A. Blais, M. H. Devoret, S. M. Girvin, and R. J. Schoelkopf, Charge-insensitive qubit design derived from the Cooper pair box, Phys. Rev. A **76**, 042319 (2007).

[40] R. Barends, J. Kelly, A. Megrant, D. Sank, E. Jeffrey, Y. Chen, Y. Yin, B. Chiaro, J. Mutus, C. Neill, *et al.*, Coherent Josephson qubit suitable for scalable quantum integrated circuits, Phys. Rev. Lett. **111**, 080502 (2013).

[41] D. Schuster, A. Wallraff, A. Blais, L. Frunzio, R.-S. Huang, J. Majer, S. Girvin, and R. Schoelkopf, ac Stark shift and dephasing of a superconducting qubit strongly coupled to a cavity field, Phys. Rev. Lett. **94**, 123602 (2005).

[42] H. Paik, D. I. Schuster, L. S. Bishop, G. Kirchmair, G. Catelani, A. P. Sears, B. Johnson, M. Reagor, L. Frunzio, L. I. Glazman, *et al.*, Observation of high coherence in Josephson junction qubits measured in a three-dimensional circuit QED architecture, Phys. Rev. Lett. **107**, 240501 (2011).

[43] P. Berman, L. Yan, K.-H. Chiam, and R. Sung, Nonadiabatic transitions in a two-level quantum system: Pulse-shape dependence of the transition probability for a two-level atom driven by a pulsed radiation field, Phys. Rev. A **57**, 79 (1998).

[44] K. A. Fischer, L. Hanschke, M. Kremser, J. J. Finley, K. Müller, and J. Vučković, Pulsed Rabi oscillations in quantum two-level systems: Beyond the area theorem, Quantum Sci. Technol. **3**, 014006 (2017).

[45] I. I. Boradjiev and N. V. Vitanov, Control of qubits by shaped pulses of finite duration, Phys. Rev. A **88**, 013402 (2013).

[46] P. Rebentrost and F. K. Wilhelm, Optimal control of a leaking qubit, Phys. Rev. B **79**, 060507 (2009).

[47] M. Carroll, S. Rosenblatt, P. Jurcevic, I. Lauer, and A. Kandala, Dynamics of superconducting qubit relaxation times, npj Quantum Inf. **8**, 1 (2022).

[48] S. Schlör, J. Lisenfeld, C. Müller, A. Bilmes, A. Schneider, D. P. Pappas, A. V. Ustinov, and M. Weides, Correlating decoherence in transmon qubits: Low frequency noise by single fluctuators, Phys. Rev. Lett. **123**, 190502 (2019).

[49] J. J. Burnett, A. Bengtsson, M. Scigliuzzo, D. Niepce, M. Kudra, P. Delsing, and J. Bylander, Decoherence benchmarking of superconducting qubits, npj Quantum Inf. **5**, 1 (2019).

[50] C. Wang, C. Axline, Y. Y. Gao, T. Brecht, Y. Chu, L. Frunzio, M. Devoret, and R. J. Schoelkopf, Surface participation and dielectric loss in superconducting qubits, Appl. Phys. Lett. **107**, 162601 (2015).

[51] A. M. Zagoskin, S. Ashhab, J. R. Johansson, and F. Nori, Quantum two-level systems in Josephson junctions as naturally formed qubits, Phys. Rev. Lett. **97**, 077001 (2006).

[52] J. Lisenfeld, G. J. Grabovskij, C. Müller, J. H. Cole, G. Weiss, and A. V. Ustinov, Observation of directly interacting coherent two-level systems in an amorphous material, Nat. Commun. **6**, 1 (2015).

[53] A. Dunsworth, R. Barends, Y. Chen, Z. Chen, B. Chiaro, A. Fowler, B. Foxen, E. Jeffrey, J. Kelly, P. Klimov, *et al.*, A method for building low loss multi-layer wiring for superconducting microwave devices, Appl. Phys. Lett. **112**, 063502 (2018).

[54] A. Bilmes, A. Megrant, P. Klimov, G. Weiss, J. M. Martinis, A. V. Ustinov, and J. Lisenfeld, Resolving the positions of defects in superconducting quantum bits, Sci. Rep. **10**, 1 (2020).

[55] X. Jin, A. Kamal, A. Sears, T. Gudmundsen, D. Hover, J. Miloshi, R. Slattery, F. Yan, J. Yoder, T. Orlando, *et al.*,

Thermal and residual excited-state population in a 3D transmon qubit, Phys. Rev. Lett. **114**, 240501 (2015).

[56] S. Shu, N. Klimovich, B. H. Eom, A. D. Beyer, R. B. Thakur, H. G. Leduc, and P. K. Day, Nonlinearity and wide-band parametric amplification in a (Nb,Ti)N microstrip transmission line, Phys. Rev. Res. **3**, 023184 (2021).

[57] D. Banys, M. A. McCulloch, S. Azzoni, B. Cooper, A. J. May, S. J. Melhuish, L. Piccirillo, and J. Wenninger, Parametric amplification at Ka band via nonlinear dynamics in superconducting 3D cavities, J. Low Temp. Phys. **200**, 295 (2020).

[58] A. D. Córcoles, J. M. Chow, J. M. Gambetta, C. Rigetti, J. R. Rozen, G. A. Keefe, M. Beth Rothwell, M. B. Ketchen, and M. Steffen, Protecting superconducting qubits from radiation, Appl. Phys. Lett. **99**, 181906 (2011).

[59] J. Lisenfeld, A. Lukashenko, M. Ansmann, J. Martinis, and A. Ustinov, Temperature dependence of coherent oscillations in Josephson phase qubits, Phys. Rev. Lett. **99**, 170504 (2007).

[60] M. Reagor, W. Pfaff, C. Axline, R. W. Heeres, N. Ofek, K. Sliwa, E. Holland, C. Wang, J. Blumoff, K. Chou, M. J. Hatridge, L. Frunzio, M. H. Devoret, L. Jiang, and R. J. Schoelkopf, Quantum memory with millisecond coherence in circuit QED, Phys. Rev. B **94**, 014506 (2016).

[61] K. W. Murch, S. J. Weber, E. M. Levenson-Falk, R. Vijay, and I. Siddiqi, $1/f$ noise of Josephson-junction-embedded microwave resonators at single photon energies and millikelvin temperatures, Appl. Phys. Lett. **100**, 142601 (2012).

[62] J. Thomas III and L. Hammer, An x-ray photoelectron spectroscopy study of sulfur hexafluoride etchant residue on silicon and silicon dioxide, J. Vac. Sci. Technol. B: Microelectron. Process. Phenom. **5**, 1617 (1987).

[63] W. M. Lee, Method for removing etching residue using a hydroxylamine-containing composition (1996), U.S. Patent 5,482,566.

[64] W. M. Lee, K. Ip, X.-D. Dinh, and D. J. Maloney, Semiconductor process residue removal composition and process (2004), U.S. Patent 6,825,156.

[65] D. C. Ford, L. D. Cooley, and D. N. Seidman, Suppression of hydride precipitates in niobium superconducting radiofrequency cavities, Supercond. Sci. Technol. **26**, 105003 (2013).

[66] N. M. Jisrawi, M. W. Ruckman, T. R. Thurston, G. Reisfeld, M. Weinert, M. Strongin, and M. Gurvitch, Reversible depression in the T_c of thin Nb films due to enhanced hydrogen adsorption, Phys. Rev. B **58**, 6585 (1998).

[67] S. Morohashi and S. Hasuo, Experimental investigations and analysis for high-quality Nb/Al-AlO$_x$/Nb Josephson junctions, J. Appl. Phys. **61**, 4835 (1987).

[68] S. P. Muraka, M. Eizenberg, and A. K. Sinha, *Interlayer Dielectrics for Semiconductor Technologies* (Academic Press, San Diego, 2003), Vol. 1.

[69] V. Ambegaokar and A. Baratoff, Tunneling between superconductors, Phys. Rev. Lett. **10**, 486 (1963).

[70] S. Huang, B. Lienhard, G. Calusine, A. Vepsäläinen, J. Braumüller, D. K. Kim, A. J. Melville, B. M. Niedzielski, J. L. Yoder, B. Kannan, *et al.*, Microwave package design for superconducting quantum processors, PRX Quantum **2**, 020306 (2021).

[71] I. J. Bahl, *Lumped Elements for RF and Microwave Circuits* (Artech House, Norwood, 2003).

[72] J. Wenner, M. Neeley, R. C. Bialczak, M. Lenander, E. Lucero, A. D. O'Connell, D. Sank, H. Wang, M. Weides, A. N. Cleland, and J. M. Martinis, Wirebond crosstalk and cavity modes in large chip mounts for superconducting, Supercond. Sci. Technol. **24**, 065001 (2011).

[73] L. Stefanazzi, K. Treptow, N. Wilcer, C. Stoughton, C. Bradford, S. Uemura, S. Zorzetti, S. Montella, G. Cancelo, S. Sussman, *et al.*, The QICK (quantum instrumentation control kit): Readout and control for qubits and detectors, Rev. Sci. Instrum. **93**, 044709 (2022).

[74] K. Serniak, S. Diamond, M. Hays, V. Fatemi, S. Shankar, L. Frunzio, R. J. Schoelkopf, and M. H. Devoret, Direct dispersive monitoring of charge parity in offset-charge-sensitive transmons, Phys. Rev. Appl. **12**, 014052 (2019).

[75] M. McEwen, L. Faoro, K. Arya, A. Dunsworth, T. Huang, S. Kim, B. Burkett, A. Fowler, F. Arute, J. C. Bardin, *et al.*, Resolving catastrophic error bursts from cosmic rays in large arrays of superconducting qubits, Nat. Phys. **18**, 107 (2022).

[76] C. H. Liu, D. C. Harrison, S. Patel, C. D. Wilen, O. Rafferty, A. Shearrow, A. Ballard, V. Iaia, J. Ku, B. L. T. Plourde, and R. McDermott, Quasiparticle poisoning of superconducting qubits from resonant absorption of pair-breaking photons, Phys. Rev. Lett. **132**, 017001 (2024).

[77] C. D. Wilen, S. Abdullah, N. A. Kurinsky, C. Stanford, L. Cardani, G. D'Imperio, C. Tomei, L. Faoro, L. B. Ioffe, C. H. Liu, A. Opremcak, B. G. Christensen, J. L. DuBois, and R. McDermott, Correlated charge noise and relaxation errors in superconducting qubits, Nature **594**, 369 (2021).

[78] L. Glazman and G. Catelani, Bogoliubov quasiparticles in superconducting qubits, SciPost Phys. Lect. Notes 31 (2021).